Static and dynamic two-dimensional patterns in self-extinguishing discharge avalanches

W. Breazeal, K. M. Flynn, and E. G. Gwinn
Department of Physics, University of California, Santa Barbara, California 93106
(Received 2 June 1994; revised manuscript received 3 April 1995)

We present experimental studies of the rich variety of two-dimensional current-density patterns that form in self-extinguishing or "silent" gas discharges between insulated, planar electrodes. Steady-state conditions evolve over seconds in this system, making it well suited for studies of the dynamics of nonequilibrium patterns. Because the patterns arise from nonlinear charge conduction processes in gases, the type of pattern obtained for a given set of bias parameters depends on the gas composition. While time-independent, Turing patterns are predominant in nearly pure He for the gap height used here, we find that adding H_2O vapor as an impurity gas produces several types of patterns with persistent time dependence. As the drive frequency is lowered, patterns with noisy space and time dependence become increasingly common. This probably reflects an enhanced effect of space-charge fluctuations on the discharge initiation sites.

PACS number(s): 82.40.Ck, 05.60.+w, 47.54.+r, 52.80.−s

I. INTRODUCTION

Pattern formation occurs when the microscopic components of a large system interact in such a way that a macroscopic ordering emerges. The phenomenon of pattern formation is extremely widespread and includes, for example, the formation of convection rolls in fluid systems [1], the cooperative or competitive growth behavior in bacterial colonies [2], and the Turing patterns recently observed in nonequilibrium chemical reactions [3]. These and other nonequilibrium systems have been the subject of extensive research over the past two decades [4].

We report studies of patterns in the visible light emitted from a gas that is made conducting by large electric fields. The self-extinguishing discharge avalanches that produce the patterns occur in near-atmospheric pressure gases that fill a narrow gap between planar, dielectric-line electrodes. For appropriate ranges of the experimental control parameters, regions of high- and low-current density form in the gas and arrange themselves into a number of different light-emitting two-dimensional patterns [5–7]. This spatially nonuniform breakdown, which is called a "silent" discharge [8], has been observed in many different gases and has applications in industrial ozone production [9,10] and in uv photochemistry [11,12].

In silent discharges, nonlinearities in charge transport in gases, and the special boundary conditions at the dielectric-lined electrodes, produce the extremely rich variety of static and time-dependent, two-dimensional patterns that we have observed, some of which have been reported previously by other authors [13,14]. Below we discuss the conditions under which time-independent Turing patterns are observed in silent discharges and compare the experimental bifurcation sequences to some of those found in simple amplitude equation models of time-independent patterns in nonequilibrium systems [4].

Because the time scales in the silent discharge allow pattern selection to take place over seconds, they are particularly well suited to studies of the *dynamics* of far-from-equilibrium patterns (for comparison, in fluid convection and nonequilibrium chemical reactions, hours or days may be required to reach a steady state). Here, we report the observation of a variety of time-dependent patterns when H_2O vapor is added to the main gas constituent, He. As the drive frequency is lowered, patterns with random components in both space and time become increasingly common. We believe that this is due to the increasing importance of fluctuations in the space charge that accompanies the light-emitting patterns in this system. These disordered patterns are similar to those found in recent mesoscopic simulations of reaction-diffusion systems [15], in which fluctuations also play an important role.

Many of the patterns we have observed resemble those found in other spatially extended, nonequilibrium systems (e.g., fluid convection [1] and nonequilibrium chemical reactions [16]). This is all the more interesting when one considers some of the significant differences between the physical mechanisms that govern these systems. For example, patterns in fluids and in nonequilibrium chemical reactions evolve under the influence of local interactions, while in silent discharges, long range space-charge fields play an important role in producing spatially nonuniform conduction. The similarity in the patterns these very different systems display suggests that the patterns should be understandable in terms of models that do not include all of the details of the fundamental dynamical equations, and that for certain ranges of the control parameters, the appropriate, simplified models may belong to the same universality class.

In the following we describe the experimental setup in Sec. II. Section III discusses charge transport in gases, and the qualitative features of the special geometry and boundary conditions used in silent discharges that lead to the formation of patterns in the current density. Section IV defines the gap compositions and gap heights used in the experiment. Section V presents the static patterns that dominate in nearly pure He, along with phase dia-

grams that show how the pattern symmetry and wavelength vary with the bias voltage and frequency. Section VI discusses the various types of time-dependent patterns that appear as water vapor is added to the main gas constituent, He, including the disordered patterns found for low-frequency drive.

II. EXPERIMENTAL SYSTEM

The silent-discharge cell consists of a gas layer sandwiched between a pair of dielectric-lined, transparent electrodes. The visible light patterns that we record are produced by repetitive, transient breakdown of the gas, initiated by an alternating-polarity voltage bias to the electrodes. Because the density of excited species increases with the current density in the gas, patterns in the current density produce the corresponding light-intensity patterns that we record through the transparent electrodes. The overlap of the upper and lower 7 mm diameter circular electrodes defines the active discharge area.

Figure 1(a) shows a schematic side view of the cell. The electrodes are lined with glass sheets with thickness $h = 125$ μm and dielectric constant $\varepsilon_i \cong 6\varepsilon_0$ [17]. Using glass shims, the plate spacing is set to a separation d (125 μm, unless otherwise noted), which is much smaller than the lateral dimensions of the electrodes. This geometry inhibits the formation of the branched, dendritic "lightning bolt" patterns that have been studied in transient discharge experiments [18] in other geometries. A square-wave voltage bias, provided by the amplified output of a programmable waveform generator, drives the transparent electrodes. Driving the electrodes with a sinusoidal bias gives results similar to the square wave used here, with poorer contrast in the visible light intensity between the low- and high-current parts of the discharge.

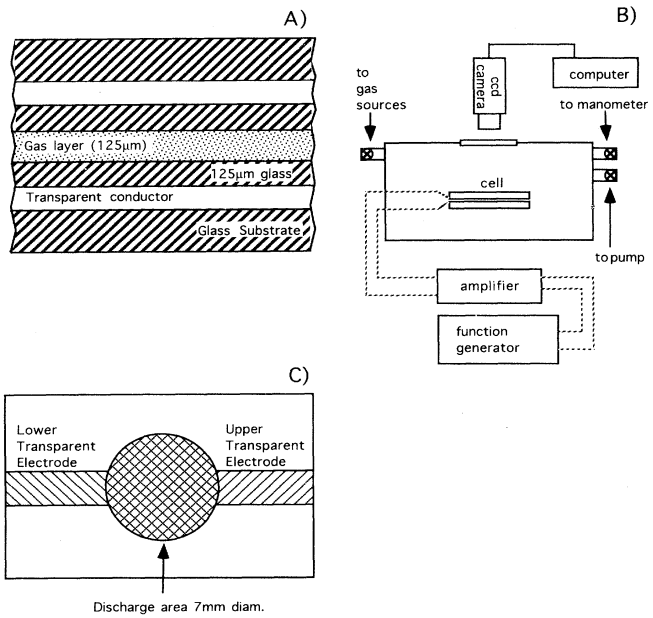

FIG. 1. Schematic of experimental setup. (a) Side view of silent discharge cell. (b) Diagram of gas box, bias circuitry, and image-collection setup. (c) Top view of experimental cell. The overlap of the transparent electrodes (indium-tin-oxide) defines the discharge region and is shown as a shaded circular area. The electrodes can also be moved laterally to produce the noncircular discharge areas used in Figs. 6(b) and 6(c), and in Fig. 10.

When the peak, total electric field in the gas, E_{gas}, is large enough, current flows in the gas between the insulated electrodes. This current excites the atoms and molecules that emit the visible light viewed with a CCD camera through the electrodes [Fig. 1(b)]. The camera has a frame rate of 30 per second and an aperture time of 1/30th of a second, so that for typical drive frequencies, the images recorded average over many drive cycles. The top view of the cell in Fig. 1(c) shows what the camera sees. Although the light intensity from the silent discharge is also nonuniform in the direction perpendicular to the electrodes, the ratio of the electrode diameter to the gap height is ~ 50 or greater, so the lateral patterns we study are essentially two dimensional. The images we collect through the transparent electrodes integrate any vertical structure in the discharge.

Because the cell's boundaries are open, the gas composition between the plates is the same as in the surrounding sealed box. The gas mixture is prepared by evacuating this box, backfilling it with a small amount of water vapor, and then adding high purity He gas.

III. NONLINEAR CHARGE TRANSPORT IN THE SILENT DISCHARGE

Silent discharges occur in electric fields that give electrons sufficient kinetic energy to break down the gas by impact ionization [8,19]. Because the kinetic energy that electrons gain from the field is limited by their inelastic collisions with the gas, which occur at a rate that increases with the gas density n_0, the scale for the electron energy in the silent discharge is set by the reduced field ratio E/n_0. For the fields in the gas in our experiments E/n_0 reaches ~ 800 Td (1 Td equals 10^{-17} V/cm^2), sufficient to break down most gases for the gap heights and pressures that we use [20,21]. In such large fields, the free electron energy greatly exceeds the thermal energy of the ions and neutral particles, so that silent discharges produce a dilute, far-from-equilibrium plasma, with typical values for the electron density of [8,19] $n_e \sim 10^{13}$–10^{14} cm^{-3}.

The basic laws that govern the silent discharge are the equations of continuity for the electrons and ions and Maxwell's equation for the divergence of the electric field. For the simple case of a gas with only one species of ion, these equations are [22]

$$\partial n_e/\partial t = -\nabla\cdot(n_e \mathbf{v}_e - D_e \nabla n_e) + \alpha n_e v_e - R n_e n_+ , \quad (1a)$$

$$\partial n_+/\partial t = -\nabla\cdot(n_+ \mathbf{v}_+ - D_+ \nabla n_+) + \alpha n_e v_e - R n_e n_+ , \quad (1b)$$

$$\nabla\cdot\mathbf{E} = e(n_+ - n_e)/\varepsilon_0 , \quad (1c)$$

where α is the electron impact-ionization coefficient, R is the recombination coefficient, n_e and n_+ are the number densities of the electrons and positive ions, respectively

[23], and $\mathbf{v}_e$, $\mathbf{v}_+$, D_e, and D_+ are their drift velocities and diffusion coefficients. Because the drift velocities, α and R are strong functions of the electric field, conduction in the gas is highly non-Ohmic. Equations (1) assume that the magnetic fields generated by the flowing charge have a negligible effect, and also neglect volume photochemical processes. In gases with more than one kind of positive ion, an additional continuity equation would be required for each species. In attaching gases (e.g., CO_2), the formation of negative ions [24] requires an additional loss term in Eq. (1a), and continuity equations for each negative species. Here, the boundary conditions that accompany Eqs. (1) are that the voltage bias applied to the electrodes $V_b = \int \mathbf{E}\cdot d\mathbf{s}$ from the positive to the negative electrode, and that no particles cross the surface of the dielectric sheets [19].

Because the time scales for electron and ion motion are quite different, numerical simulations of the nonlinear, dissipative partial differential equations in (1), with the above boundary conditions, are extremely slow. Simulations have been made for silent discharges only in two space dimensions (the dimension normal to the insulated electrodes and one lateral dimension), for small lateral lengths that contain a single discharge avalanche [25]. Because there have been no numerical studies of the two-dimensional (2D) discharge patterns discussed here, a detailed picture of the dependence of the pattern form on the parameters in Eqs. (1) is not available. However, the qualitative factors that favor laterally nonuniform current flow in silent discharges, which are electron avalanches in the gas, coupled with the space charge fields produced by charge accumulation on the dielectric surfaces, are discussed below.

Figure 2 illustrates the processes that occur in the silent discharge during a cycle of a square-wave bias voltage of amplitude V_b. As shown in Fig. 2(a), charge flows in the gas during short [10,26], submicrosecond pulses that start just after the bias voltage reverses sign (for simplicity, Fig. 2(b) assumes laterally uniform current flow in the gas). This current causes electrons to accumulate on the dielectric sheet over the anode, and ions to accumulate on the dielectric over the cathode [left-hand side of Fig. 2(b)]. So, the total electric field $E_{\rm gas}$ is a combination of the electric field $E_{\rm bias}$ produced by the charges on the anode and cathode and the field $E_{\rm sc}$ produced by the space charge that collects on the dielectric surfaces. As the discharge progresses, the space-charge field $E_{\rm sc}$ reduces $E_{\rm gas}$ until loss processes such as electron attachment outstrip ionization, and the current in the gas falls to zero. For current pulses that transfer a uniform sheet charge density $+\sigma_g$ onto the cathode, and $-\sigma_g$ onto the anode [left-hand side, Fig. 2(b)], the magnitude of the field in the gas just *after* the current pulse is approximately [27]

$$E_{\rm gas} = (V_b \varepsilon_i - 2h\sigma_g)/(d\varepsilon_i + 2h\varepsilon_0) \ . \tag{2a}$$

Here, ε_i is the dielectric constant of the glass insulating layers ($\sim 6\varepsilon_0$), d is the gap height, and h is the thickness of the dielectric layer. The electric field $E_{\rm bias}/\varepsilon_i$ in the dielectric layers increases as charge collects on the dielectric layers in response to the decrease in $E_{\rm gas}$ produced by a current pulse. Thus, just after a current pulse, most of V_b drops across the dielectric layers. When the bias voltage reverses, the space-charge field $E_{\rm sc}$ *reinforces* the field $E_{\rm bias}$, as sketched on the right-hand side of Fig. 2(b), so that just after the bias voltage changes sign, the field in the gas is approximately

$$E_{\rm gas} = (V_b \varepsilon_i + 2h\sigma_g)/(d\varepsilon_i + 2h\varepsilon_0) \ , \tag{2b}$$

where loss processes (e.g., recombination) during the zero-current part of the previous half cycle have been neglected. This enhanced field at the beginning of the new half cycle initiates a new current pulse, which transfers charge across the cell until the opposing space-charge field once again extinguishes the particle current across the gap. The enhancement of $E_{\rm gas}$ by the space-charge field at the beginning of each current pulse makes the bias voltage required to maintain the silent discharge substan-

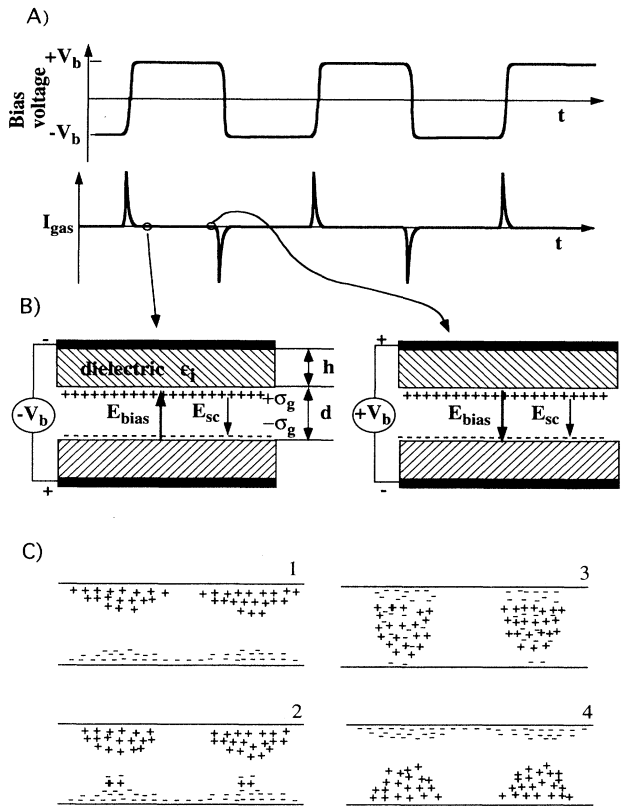

FIG. 2. The current in the gas flows in submicrosecond, self-extinguishing current pulses that transfer a sheet charge density σ_g across the gap. (a) Bias waveform applied to the electrodes, and corresponding current pulses in the gas. (b) Space charge field $E_{\rm sc}$, bias field $E_{\rm bias}$, and transferred sheet charge density σ_g just *after* a current pulse (left-hand side) and just before a current pulse begins (right-hand side), for the case of laterally uniform σ_g. Here h is the thickness of the dielectric layer and d is the gap height. (c) Sketch of evolution of space-charge distribution during a current pulse. (1),(2) initial stages of current discharge; (3) impact-ionization avalanche; (4) end of current pulse.

tially less than the bias voltage required to first initiate it, because the space-charge fields are absent until the first current pulse.

The relative sizes of E_{sc} and E_{bias} can be estimated from the particle current I_{gas} that flows in the gas during a current pulse. We find I_{gas} by measuring the total current $I_{gas}+I_{dis}$ in the electrode leads with a current-sensitive probe and a digital storage oscilloscope, and then subtract the displacement current contribution due to charging the electrodes, I_{dis}, which we measure for the same bias waveform in the evacuated cell. The transferred sheet charge density σ_g is approximately $\sigma_g=[\int I_{gas}(t)dt]/A$, where A is the total lateral area filled with a bright discharge. Using this estimate of σ_g in Eq. (2b) gives a space-charge field E_{sc} comparable to E_{bias}.

For a range of bias parameters, current flow in the gas is laterally nonuniform, as illustrated schematically in Fig. 2(c) for times during one discharge avalanche. The tendency of silent discharges to form such laterally *inhomogeneous* current and transferred charge densities stems from the impact-ionization mechanism [28,29] for current flow in the gas. Consider a fluctuation that produces a local enhancement, Δn_e, in the free electron density, as sketched in Fig. 3. The superposition of the field E_{bias} and the space-charge field $E_{\Delta n_e}$ from this region of excess electron density makes the total field E_{gas} largest in the direction of electron drift just in front of Δn_e. Because the impact-ionization coefficient α in Eqs. (1) is a rapidly increasing function [22,30] of E, the rate of free electron production reaches a maximum just in front of Δn_e, so that the electron avalanche will travel toward the anode much more rapidly than it spreads laterally. Thus, the avalanche tends to punch through the gas along a spreading, needlelike path [31], and the cross section of *isolated* avalanches initiated by a localized "seed" electron distribution is circular [32] for small gap heights d. When the avalanche runs into the dielectric over the anode, electrons accumulate in a patch on the dielectric surface. The ions produced by the avalanche travel (much more slowly) to the dielectric over the cathode, where they produce a patch of excess positive charge, in the same lateral region as the electrons. Thus, the focusing of the impact-ionization avalanche along the direction of the field E_{bias} produces localized regions of large σ_g on the dielectric surfaces. These regions of large σ_g tend to remain in the same location on the dielectric surfaces from cycle to cycle, because current flow across the gap is enhanced where E_{gas} at the start of a current pulse is largest, and because the maximum value of the normal component of the field at the beginning of a current pulse occurs where the charge density transferred in the previous half cycle is largest. As V_b increases, the peak, total field in the gas also rises, and the area occupied by a high-current avalanche tends to grow.

We have observed that lateral variations in the current density appear in the silent discharge only over a range of fields in the gas. If E_{gas} is too small, no current flows. For large enough E_{gas}, the entire discharge area breaks down, so that in this high-field limit, a laterally uniform, bright glow is emitted from the cell. The existence of an intermediate field range over which current flow is laterally nonuniform is typical in bulk materials with avalanche current flow, such as gases and semiconductors [33], which can have bistable, S-shaped current density field characteristics. This is illustrated qualitatively in Fig. 4, which shows how low- and high-current-density regions can coexist, as may be relevant to silent discharges. For E_{gas} below a threshold field E_{th}, the J-E characteristic is single valued, and the current density is small and uniform. For $E_{gas}>E_{uni}$, the J-E characteristic is also single valued, and the current density is large and uniform. If E_{gas} is in the bistable region between E_{th} and E_{uni}, charge flow can break up spatially into regions of high- and low-current density, corresponding to each of the two stable branches of the J-E curve (solid lines in Fig. 4). As discussed above, in silent discharges the space charge produced by the discharge avalanches is important in the pattern selection process in such an intermedi-

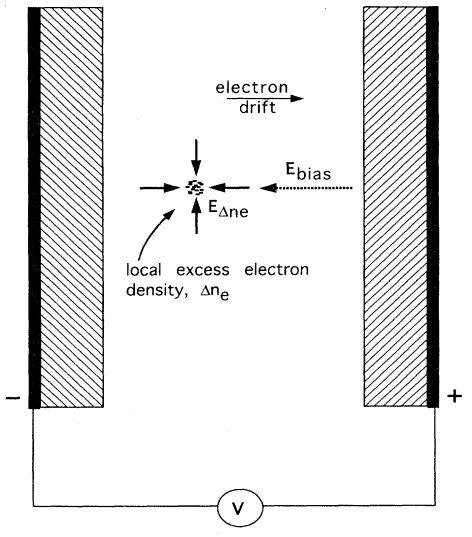

FIG. 3. Enhancement of the total field E_{gas} just in front of a region of excess electron density, Δn_e, at the head of an avalanche. In the direction of electron drift, $E_{\Delta n_e}$ reinforces E_{bias}, so that the avalanche spreads faster in the direction normal to the electrodes than in the lateral directions.

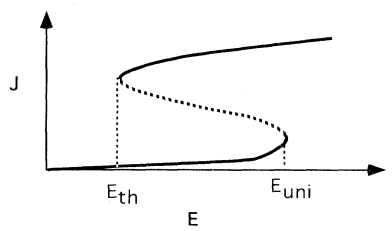

FIG. 4. Bistable J vs E characteristic. If E_{gas} is below E_{th}, no discharge occurs; and if E_{gas} is above E_{uni}, a laterally uniform discharge forms. E_{gas} in the bistable region allows current flow in the gas to become laterally nonuniform.

ate field regime, because space-charge fields contribute to the electric field in the gas. The arrangement of the space charge near the dielectric surfaces depends on how the current density varies laterally and produces large spatial variations in E_{gas} both laterally and in the direction normal to the electrodes.

As mentioned in the Introduction, an important experimental advantage of silent discharges for studies of 2D patterns is the convenient time scale over which steady-state behavior is reached after changing a control parameter. These times are much longer than the duration of the discharge current pulses, in part because the charge transferred across the gap during a current pulse stabilizes gradually over many discharge cycles. This gradual approach to a constant charge transfer occurs because the more charge transferred across the gap in a current pulse, the larger the initial contribution E_{sc} makes to E_{gas} on the subsequent half cycle of the drive. This tends to increase the charge transferred across the gap on the next half cycle, and so on. A steady situation is eventually reached when the enhancement in the charge transfer due to the space-charge fields balances the decay in the space charge between current pulses.

In small-area silent discharge cells with aspect ratios $L/d \sim 1$, roughly 10 drive cycles are required for the current pulses to reach a steady state in which they transfer the same charge on each half cycle of the drive [34]. In such small-area cells, the space-charge field is not weakened significantly by lateral charge drift and diffusion between current pulses. In contrast, for large-area electrodes with dimension $L \gg d$, lateral inhomogeneities in the transferred charge smooth by drift and diffusion during the time between current pulses over a time scale at Δt_{smooth} that is presumably dominated by the slower motion of the ions [35]. This Δt_{smooth} should determine the characteristic times for pattern rearrangements in the large-area silent discharges we study. For the conditions of our experiments, Δt_{smooth} appears to be very roughly on the order of 1–10 msec based on the ~ 100–1000 Hz drive frequency at which the locations of discharge regions of size $\sim d$ begin to be correlated in time [36]. For the $L/d \sim 100$ aspect ratio cells that we have studied so far (L is the electrode diameter), transient rearrangements in patterns typically persist for ~ 1 sec, or about $(100\text{–}1000) \times \Delta t_{smooth}$.

IV. EFFECTS OF VARYING THE GAS COMPOSITION AND PRESSURE

Because the gas composition determines the electric-field- and pressure-dependent transport coefficients that govern charge flow in Eqs. (1), the patterns formed by silent discharges are sensitive to the gas mixture that fills the gap between the dielectric-lined electrodes. For the range of experimental control parameters that we have used, the only conducting state observed in pure He gas is laterally uniform, although patterned states may appear for pressures and field regimes that we have not studied. We access patterned conducting states by adding water vapor to He and specify the amount of water vapor in the gas mixture as the ratio of the H_2O vapor pressure initially introduced into the evacuated cell, P_{H_2O}, to the final, total pressure of the He-H_2O mixture. The water vapor concentrations, total gas pressures, and gap heights that we have found to produce distinct classes of time-dependent patterns are denoted as levels I–IV which respectively correspond to water vapor concentrations of $<0.0086\%$, a total pressure of ~ 700 Torr, and $d = 75$ μm (level I); water vapor concentrations of 0.067–0.27%, a total pressure of 300 Torr, and $d = 125$ μm (level II); water vapor concentrations of 0.27–0.4%, a total pressure of 300 Torr, and $d = 125$ μm (level III); and water vapor concentrations of $\sim 0.57\%$, a total pressure of 700 Torr, and $d = 75$ μm (level IV).

Figure 5 shows that, in addition to producing patterned conducting states, adding H_2O vapor to the cell increases the bias voltage required to maintain current flow in the gas. The data in Fig. 5 were obtained by ramping V_b to 420 V, a value substantially larger than that required to initiate current flow, and then gradually reducing V_b until the current is extinguished, at a bias voltage V_{off}. This process was repeated for several partial pressures of water vapor in an He-H_2O gas mixture with a total pressure of 760 Torr, at a drive frequency $f_{dr} = 80$ kHz, for a plate spacing $d = 125$ μm. The largest H_2O concentration, which corresponds to the maximum level used in the experiments discussed below, increases V_{off} by about 25% (for other frequencies and plate spacings, the effect on V_b may be different). This indicates that H_2O vapor reduces the supply of free electrons, presumably by attachment to form negative ions, so that larger fields are required to prevent the avalanche's collapse.

V. STATIC SILENT DISCHARGE PATTERNS

The states of patterned conduction that we have observed for levels I and II are static away from bifurcation

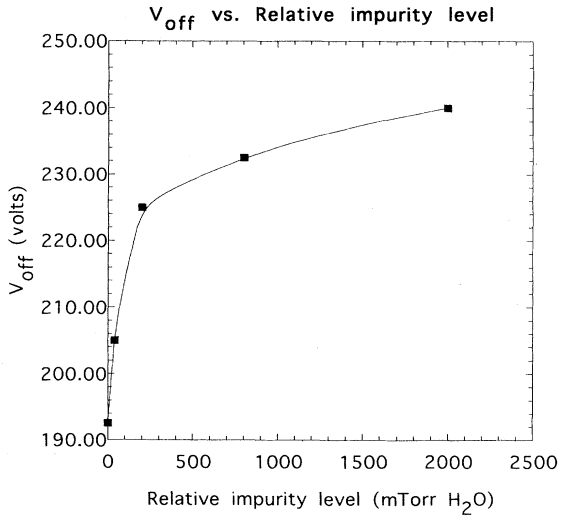

FIG. 5. Bias voltage V_{off} at which current flow ceases as the bias voltage is reduced. V_{off} increases as the H_2O vapor level increases, which suggests that electron attachment is removing free electrons from the avalanche.

points, for $f_{dr} < \sim 2000$ Hz. Here, "static" means that the pattern does not change on time scales that the eye can follow, as expected if the high-current regions reform at the same locations on each half cycle of the drive. We observe three types of time-independent patterns: a hexagonal array of high-current-density dots, a striped pattern, and an inverted hexagonal array of low-current-density dots that thread a high-current-density background. Figure 6 shows examples of these patterns for level I. In Figs. 6(b) and 6(c), the discharge area is noncircular, with a roughly rhombus-shaped inner region that connects to two, rectangular outer regions. As shown in Fig. 6(b), the stripes in this low-impurity regime tend to align parallel to the cell boundaries, where the field falls smoothly to a value below that required to maintain current flow. The slightly nonuniform gap height in Fig. 6(c) is responsible for the coexistence of the stripe and inverted hexagonal patterns, which demonstrates the sensitivity of the pattern form to the plate separation d. For all of the images shown, high brightness levels correspond to high current densities and low brightness levels correspond to low current densities. The dark spot in the upper left quadrant of some of the images is a bubble in the adhesive between the electrodes and their glass lining. Finally, it should be noted that it is possible to generate a laterally uniform conducting state, regardless of the impurity level, if a high enough voltage bias is applied, although the bias voltage required to do so increases as the amount of water vapor in the system increases.

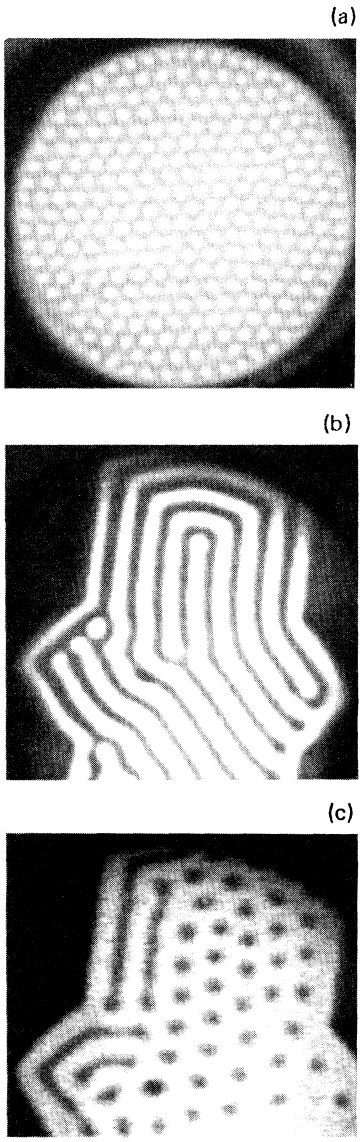

FIG. 6. Patterns formed at level I ($d = 75$ μm, $P_{He} \sim 700$ Torr, $P_{H_2O} < 60$ mTorr). The discharge area is circular in (a) and has a rhombus-shaped region between rectangular sections in (b) and (c). (a) Hexagonal pattern of bright dots ($V_b = 400$ V, $F_{dr} = 80$ kHz). (b) Stripe pattern ($V_b = 350$ V, $f_{dr} = 45$ kHz). (c) inverted hexagonal array (right-hand side) and stripes (left-hand side), for $V_b = 320$ V and $f_{dr} = 6$ kHz. The symbols within the regions correspond to the points at which data were collected.

The patterns in Fig. 6 have the same form as the Turing patterns that have been observed in experimental [16,37] and theoretical [38] studies of fluid convection and of nonequilibrium chemical reactions. More generally, hexagons and stripe patterns are commonly seen in quasi-two-dimensional systems where the inversion symmetry in the direction normal to the plane of the patterns is broken, such as non-Boussinesque convection. Models for these static, two-dimensional patterns often use the following Ginzburg-Landau "amplitude" equations to describe the system's behavior for values of the control parameters in the weakly nonlinear regime:

$$\partial_t A_1 = \varepsilon A_1 - \gamma A_2^* A_3^* - [|A_1|^2 + g_1(|A_2|^2 + |A_3|^2)] A_1 , \tag{3}$$

with cyclically permuted equations for A_2 and A_3. In Eq. (3), A_1, A_2, and A_3 are the three complex amplitudes, which correspond to the three basic stripe states that make up hexagonal patterns [4]. For fluid convection, the control parameters can be defined in terms of the fluid parameters (Rayleigh number, density, and Prandlt number). Figure 7 shows a phase diagram for this

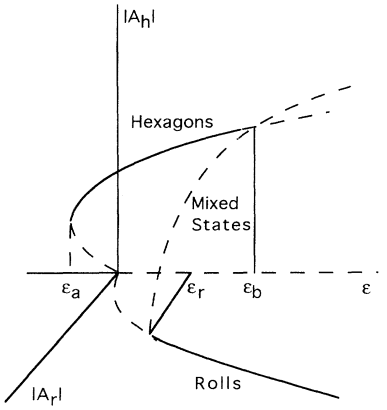

FIG. 7. A diagram of the amplitudes of the roll state $|A_r|$ and hexagon state $|A_h|$ as a function of the control parameter ε. The dashed lines correspond to unstable states, and the solid lines correspond to stable states.

set of model equations. As ε increases, they predict a subcritical transition from a uniform to a hexagonal state at $\varepsilon=\varepsilon_a$. For values of ε between ε_r and ε_b the system is bistable for stripes and hexagons, and for values of $\varepsilon>\varepsilon_b$, only rolls are stable. So, the amplitude equations for a system that displays both hexagons and stripes predict that the bifurcation sequence will be *uniform state* $\leftrightarrow$ *hexagonal pattern* $\leftrightarrow$ *striped pattern,* and that the transitions are hysteretic. In silent discharges, patterns are sensitive to the bias voltage V_b and to the drive frequency $f_{\rm dr}$ (as well as to the gas composition and pressure, and the plate spacing, which are held fixed during a given set of experiments). To study how the form of time-independent patterns in silent discharges depends on these *experimental* control parameters, we have made phase diagrams that show the type of pattern obtained for varying V_b and $f_{\rm dr}$. The experimental control parameters V_b and $f_{\rm dr}$ are used to describe the phase space, since we have no way at present to link V_b and the drive frequency to the model control parameters in Eq. (3).

Figure 8 shows a phase diagram for the form of the static patterns found at level I. The data were taken by fixing $f_{\rm dr}$, and setting the voltage to the maximum output of the amplifier used in this series of experiments (420 V), which produced the various conducting states along the top of Fig. 8. The points show the parameters at which data were taken in Figs. 8 and 9. Here, *u* stands for a uniform conducting state, *i* stands for the inverted hexagonal pattern [right-hand side of Fig. 6(c)], *s* stands for a stripe pattern [as in Fig. 6(b)], and *h* for the normal hexagonal pattern [Fig. 6(a)]. As the voltage is reduced from this maximum value, the pattern changes at certain values of V_b, by altering either its spatial frequency or its symmetry. In Fig. 8 the solid lines roughly outline the regions in parameter space that correspond to patterns with a given symmetry. These approximate phase boundaries may encompass patterns with forms different from those indicated that this coarse search through control parameter space missed. With this caveat, we find that the boundaries between different pattern types are tongue-shaped curves that extend out along the frequency axis, and that as the frequency grows, hexagonal arrays of bright dots become the dominant pattern type.

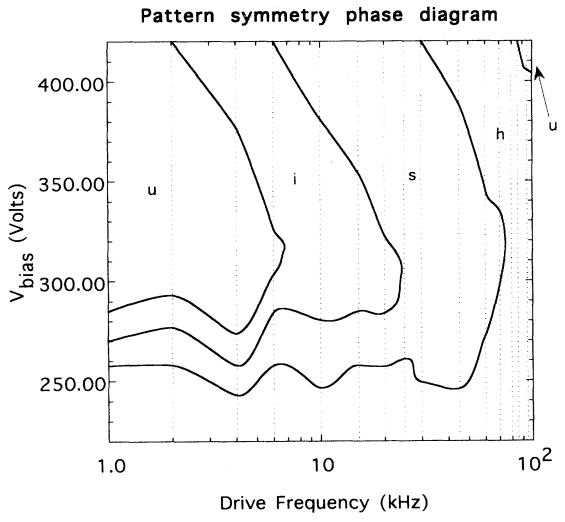

FIG. 8. Phase diagram of the pattern type as a function of bias voltage V_b and drive frequency $f_{\rm dr}$. The types of patterns seen are hexagonal arrays of dots (*h*), stripes (*s*), inverted hexagonal patterns (*i*). A uniform discharge is indicted by (*u*). For lower V_b than shown, the hexagonal dot array undergoes a transition to the nonconducting state. For higher V_b than shown, the hexagonal dot array bifurcates to a uniform conducting state. The dashed lines indicate the frequencies at which data were collected.

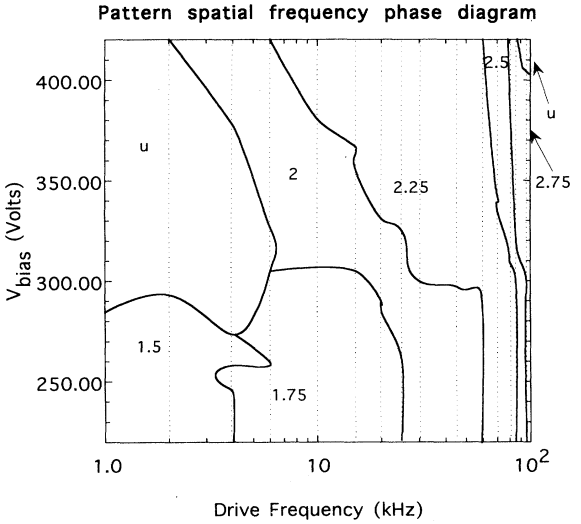

FIG. 9. Phase diagram of the pattern's spatial frequency as a function of V_b and drive frequency. The spatial frequency is measured by counting the number of pattern wavelengths per millimeter.

The bifurcation sequence predicted by the amplitude equations discussed above is consistent with the observed bifurcation sequences in the silent discharge cell obtained by varying V_b for drive frequencies below $\sim$60 kHz: we always observe the transition *uniform state* $\leftrightarrow$ *hexagonal pattern* $\leftrightarrow$ *striped pattern* and never *uniform state* $\leftrightarrow$ *striped pattern* $\leftrightarrow$ *hexagonal pattern.* Although the uniform conducting state at high voltages is not shown in Fig. 8, improvements in the high-voltage amplifier made after the data in Fig. 8 were collected allowed us to confirm that the cell breaks down uniformly at high enough V_b, and that the first patterned state observed on reducing V_b is a hexagonal array of the type shown in Fig. 6(a). Further reduction of V_b produces a stripe array at drive frequencies below $\sim$60 kHz. Thus, for wide ranges of the drive frequency, the first two bifurcations between states of different symmetry that are produced by reducing V_b follow the standard sequence. For $f_{\rm dr}$ from $\sim$20 kHz to $\sim$60 kHz, continuing to reduce V_b produces an inverse bifurcation sequence of *stripes* $\rightarrow$ *hexagonal pattern* $\rightarrow$ *uniform nonconducting state* (which lies at lower voltages than shown in Fig. 8).

As discussed earlier, the amplitude equation description also predicts that the transitions between patterns of different symmetry will be hysteretic. We have not made

a careful study of the nature of the bifurcations we have observed, but we do find hysteresis as V_b is swept up or down across the uniformly off–to–hexagonal-pattern transition. This may partly reflect hysteresis in the space-charge density on the dielectric plates. As discussed above, the electric field in the gas, E_{gas}, determines charge transport, and depends on *both* the bias field and the space-charge field. This fact alone leads to hysteresis in the voltage bias at the transition between the uniform, nonconducting state and the hexagonal conducting state because the space-charge field is absent as the voltage bias ramps up through the nonconducting state, while on a ramp down in V_b, large space-charge fields are present until the total field falls below that required to maintain current flow. We plan more detailed studies of bifurcations between pattern types, using measurements of the transferred charge to correct for this extra source of hysteresis.

Other interesting features of the phase diagram in Fig. 8 include the more complex bifurcation sequences found for low drive frequencies. For f_{dr} between ~ 5 kHz and ~ 10 kHz, reducing V_b over the voltage range shown produces the sequence *inverted hexagonal pattern* $\rightarrow$ *striped pattern* $\rightarrow$ *hexagonal pattern.* Hexagonal and inverted hexagonal patterns similar to the ones we observe have also been found in experiments and simulations on nonequilibrium chemical reactions [40]. At lower drive frequencies, we find reentrant transitions to a uniform state. For example, for $f_{dr}=5$ kHz, decreasing the voltage bias from the inverted hexagonal state produces a transition to a laterally uniform conducting state (which may actually be a patterned state that moves rapidly enough to produce an apparently uniform state over the $\frac{1}{30}$ sec aperture time of the camera). Further decrease of V_b produces a bifurcation back to the inverted hexagonal state. These more complex bifurcation sequences are reminiscent of the reentrant-hexagon–to–stripe transitions seen in thermal convection in the presence of a first-order phase change [41].

As mentioned above, varying the drive frequency and bias voltage produces transitions between patterns with different spatial frequencies, as well as the bifurcations between states with different symmetries shown in Fig. 8. At the low impurity levels that produce time-independent patterns, increasing the bias voltage or the drive frequency tends to decrease the pattern's wavelength, as shown in the spatial frequency phase diagram in Fig. 9. The spatial frequencies are determined by counting the number of pattern wavelengths across a segment of fixed width (a spatial frequency of 1 in Fig. 8 corresponds to a wavelength of 1 mm). All of the experimental control parameters in Fig. 9 are identical to those in Fig. 8.

Comparison of Fig. 8 and Fig. 9 shows that the contours for the pattern type (Fig. 8) and spatial frequency (Fig. 9) are different. While the sequence of bifurcations between pattern types shown in Fig. 8 indicates that the pattern form may be determined by minimizing a Liapunov functional, the tendency of the wavelength to fall as either V_b or f_{dr} increases implies that two factors dominate the wavelength: the transit time for an avalanche to cross the gap height d, and the length of time between current pulses. As discussed above, individual current avalanches spread as the discharge progresses across the gap. Because drift and diffusion tend to widen the avalanche's lateral extent, the longer the transit time across the cell, the more the discharge will spread. Because increasing V_b decreases the transit time, increasing V_b should also decrease the lateral extent of individual discharges, favoring the observed higher spatial frequencies. The increase in spatial frequency observed when the plate spacing is reduced is consistent with this interpretation because reducing d also reduces the transit time and the lateral extent of an isolated discharge.

As shown in Fig. 9, spatial frequency also rises with increasing drive frequency, f_{dr}. As mentioned above, the duration of a typical current pulse is less than 1 μsec. In the much longer half-drive period interval between current pulses, the space charge on the dielectric plates smoothes, so that a region of enhanced charge density produced by an individual discharge avalanche will spread more at low f_{dr} than at high f_{dr}. Since the discharges tend to reform where the space-charge density at the dielectric surfaces is large, lower drive frequencies should lead to larger discharge areas and lower spatial frequencies, as observed. This reduced smoothing of the space-charge density for short drive periods may also account for the dominance of hexagonal arrays of bright dots at high f_{dr}, for which there will be less tendency for the space-charge density from isolated discharge avalanches to spread and overlap. If this is the case, then the isolated discharge spot is the basic element that makes up the observed static patterns.

We find that for level II, the observed patterns are static for f_{dr} above ~ 500 Hz and have the same basic form as those found at level I, although with somewhat altered appearance (Fig. 10). The hexagonal pattern of dots [Fig. 10(a)] is still stable, but the lattice has more defects, probably because the circular cell boundary strongly influences the arrangement of the relatively small number of elements in this coarse pattern. The pattern of stripes [Fig. 10(b)] has a scalloped appearance. These stripes form when the regions between adjacent dots in the hexagonal array fill in, which make the stripes look like a series of beads on a string. The same filling phenomenon takes place when the stripes undergo a transition to the inverted hexagonal array [Fig. 10(c)]: the bulges along adjacent stripes merge. Thus, the underlying structure of the patterns at level II is the hexagonal dot array: the dots connect together to make up the stripe and inverted hexagonal patterns. At level II, the spatial extent of the individual discharges still strongly depends on the voltage and frequency. As discussed above, the size of the individual discharges decreases as either parameter is increased.

Increasing the water vapor concentration through level IV produces further changes in the form of the observed time-independent patterns. At moderate voltages and frequencies, increasing the impurity level slowly reduces the packing density of the hexagonal pattern. As the water vapor concentration rises further, vacancies appear in the hexagonal pattern of bright dots [Fig. 11(a)]. Increas-

ing the water vapor concentration still more produces a hexagonal pattern of vacancies, as shown at the center of Fig. 11(b). Further increases in the impurity level produces a time-dependent state that is discussed in the next section.

For H_2O impurity levels at level III and higher, the size of individual discharge spots, and the pattern's spatial frequency, become much less sensitive to the drive frequency than at lower impurity levels. This suggests that in this high-impurity regime, the processes that determine the pattern wavelength are nearly independent of the time interval between discharges, perhaps because electron attachment to form heavy, negative ions slows down the lateral smoothing of the space-charge density. The spreading of the avalanche discharge as it traverses the gap and the dipole-dipole repulsions of the separate discharge site's space charge may be the main factors that determine the spatial frequency.

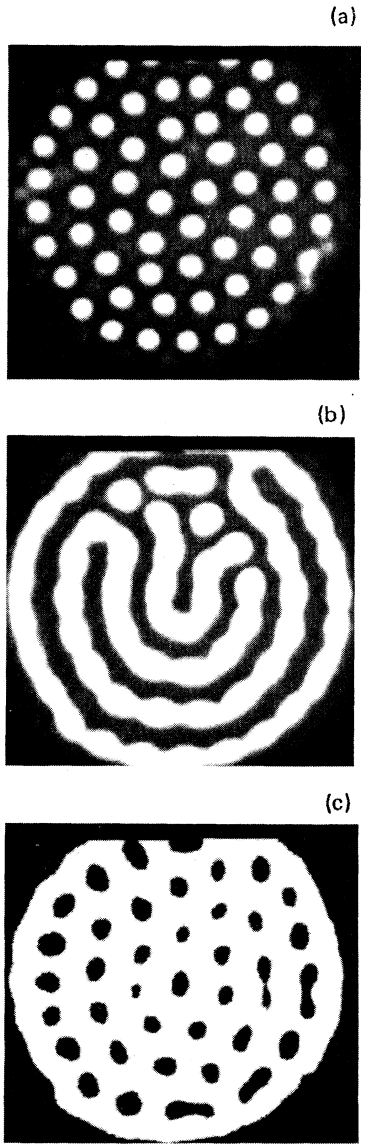

FIG. 10. Patterns at level II ($d=125$ μm, $P_{He}\sim 300$ Torr, $P_{water}=200$–800 mTorr). (a) An array of dots ($V_b=210$ V, $f_{dr}=100$ kHz). (b) Textured stripe pattern ($V_b=240$ V, $f_{dr}=100$ kHz). (c) Inverted dot array ($V_b=255$ V, $f_{dr}=100$ kHz).

VI. DYNAMIC PATTERNS IN SILENT DISCHARGES

The static patterns discussed above dominate for low water vapor impurity levels. As the fraction of water va-

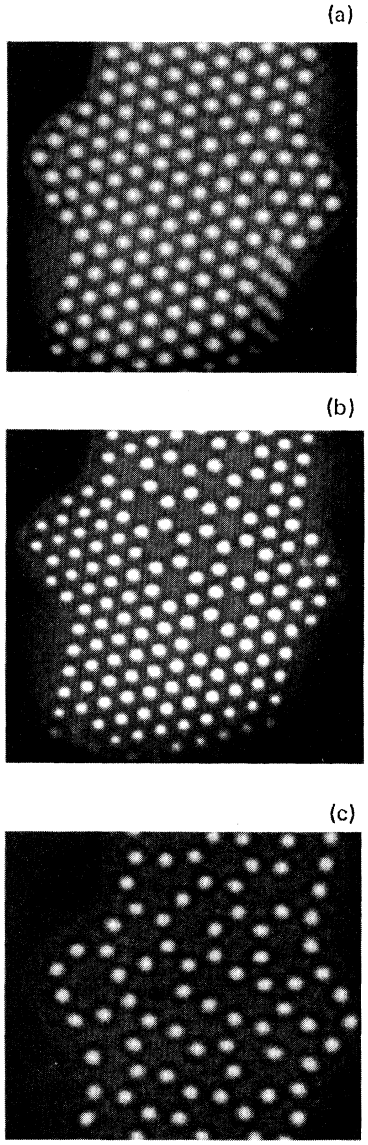

FIG. 11. New pattern types at level IV ($d=75$ μm, $P_{He}\sim 700$ Torr, $P_{water}=4$ Torr). (a)–(c) show the reduction in the number of nearest neighbors with increasing impurity level. Patterns (a) and (b) are static and pattern (c) is time dependent. (a) Vacancies appear in the upper right quadrant of the cell ($V_b=365$ V and $f_{dr}=80$ kHz). (b) An open, hexagonal array appears in the central region of the cell ($V_b=360$ V, $f_{dr}=180$ kHz. (c) Dynamic pattern of chained dots ($V_b=365$ V, $f_{dr}=80$ kHz).

por in He rises, new classes of patterns with persistent time dependence emerge. In this section, we discuss the qualitative characteristics of these patterns and the conditions under which they are observed.

Time-dependent patterns first appear at impurity level III, for example, a focus defect that emits outwardly traveling circular waves at a rate of approximately 1 per second, as shown in Fig. 12(a) for $V_b = 340$ V and $f_{dr} = 190$ kHz [the striations in Fig. 12(a) are milling marks on the Al plate beneath the lower transparent electrode and are not part of the pattern]. Target patterns of the type shown in Fig. 12(a) typically arise in systems with cylindrically symmetric boundary conditions, such as for the circular discharge cell boundaries in Fig. 12. The focus of such patterns can display interesting dynamical behavior; for example, theoretical studies of Rayleigh-Bénard convection have shown that for control parameters far enough beyond the uniform steady state's loss of stability to a centered target pattern, a symmetry-breaking instability causes the focus of the target pattern to shift away from the center of the cell [42]. It will be interesting to see whether target patterns in silent discharges display similar behavior.

We also observe a new type of dynamic, striped pattern

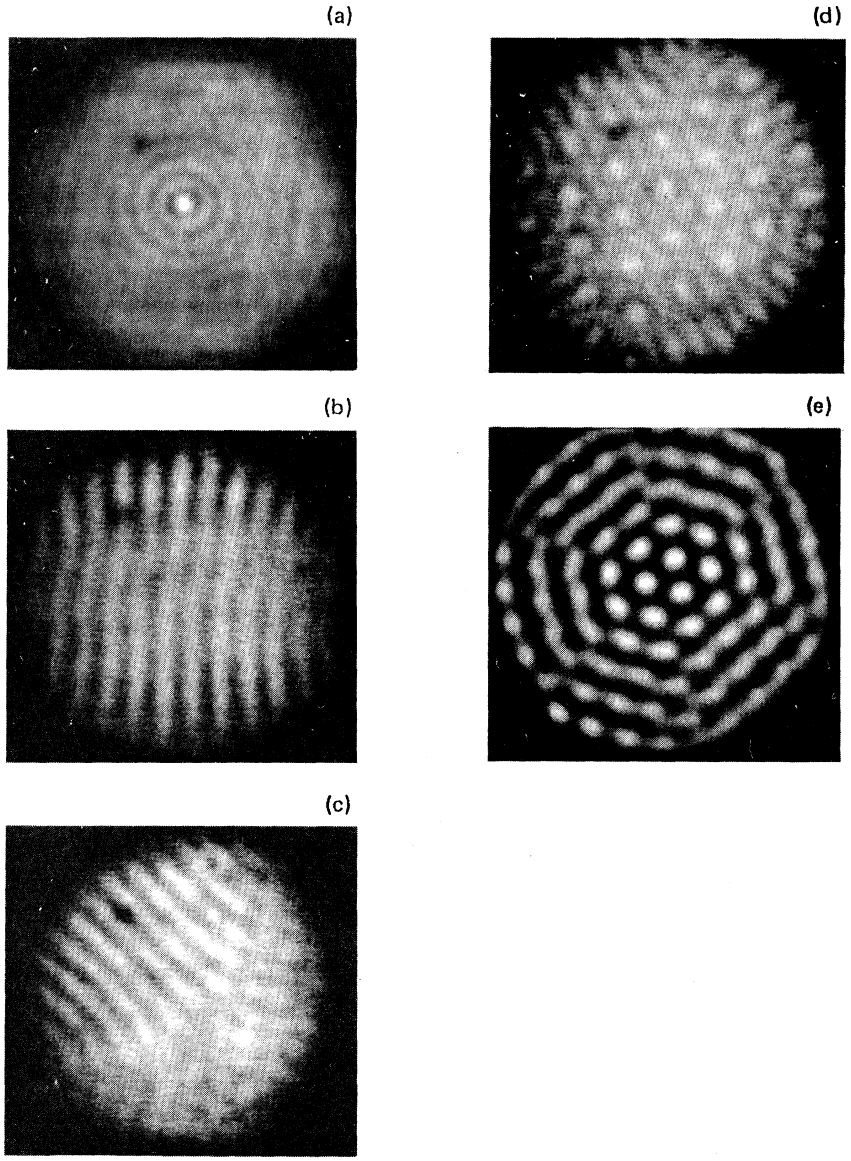

FIG. 12. Time-dependent patterns at level III ($d = 125$ μm, $P_{He} \sim 300$ Torr, $P_{water} \sim 800$ mTorr–1.2 Torr). (a) Target pattern of concentric traveling waves, which are emitted from the central focus (bright spot) for $V_b = 340$ V and $f_{dr} = 190$ kHz. (b),(c) Dynamic stripe pattern that rapidly reorients between different preferred axes ($V_b = 340$ V and $f_{dr} = 180$ kHz). (d) Dynamic, mixed pattern of stripes and dots ($V_b = 400$ V and $f_{dr} = 180$ kHz). (e) Rapidly rotating hexagonal dot pattern ($V_b = 260$ V and $f_{dr} = 180$ kHz).

at impurity level III. Figures 12(b) and 12(c) show images of this pattern taken at two different times, for $V_b = 340$ V and $f_{dr} = 180$ kHz. Although it cannot be seen clearly in the images shown, the stripes appear to align themselves normal to the (circular) boundary, in contrast to the preferred parallel orientation of the static stripes found at levels I and II. [This is not apparent in Figs. 12(b) and 12(c) because of poor contrast at the outer portions of the cell, where the eye can discern the stripe ends splaying to a normal orientation.] The orientation of the stripes changes over time, so that they appear to flicker between alignment along a set of axes separated by ~ 120 degrees (there only two orientations, probably determined by some irregularity in the cell boundary, i.e., where the straight part joins the circular part of the electrodes). The time scale for the stripes to remain in a given orientation is ~ 1 sec, with much shorter transitions between orientations. The quilted appearance of the lower right-hand side of Fig. 12(c) suggests that stripes of different orientations can be present simultaneously, and that changes in the relative amplitudes of different stripe sets produce the time evolution of the pattern.

Figures 12(d) and 12(e) show examples of two other types of time-dependent patterns that we have observed at impurity level III. Figure 12(d) ($V_b = 400$ V and $f_{dr} = 180$ kHz) is a mixed state of large dots and stripes that orient normal to the circular cell boundary. This pattern has a time dependence similar to that of the stripes in Figs. 12(b) and 12(c): it undergoes sudden rotational reorganization along a set of preferred axes separated by ~ 120 degrees. The time-dependent pattern in Fig. 12(e) ($V_b = 260$ V and $f_{dr} = 180$ kHz) appears to be made up of a set of continuously rotating dots. The rotation is clockwise and was the same for all trials. The dots at the center move slowly, so that they do not smear the image over the $\frac{1}{30}$ sec frame duration. The outer parts of the patterns appear to move at higher speeds, so that the blurred appearance in Fig. 12(e) may result from the dots' motion during the aperture time of the CCD camera.

As discussed above, increasing the impurity concentration to the low end of level IV produces voids in the static hexagonal pattern that is the most common pattern type at this high H_2O vapor level. As the concentration of water vapor increases, the static open hexagonal pattern in Fig. 11(b) evolves into a time-dependent state of rearranging clusters of distinct dots [Fig. 11(c)]. As Fig. 11(c) shows, the dots link to form linear chainlike structures. These chains rearrange themselves, by breaking and rejoining at new places, over time scales of ~ 1 sec.

At low enough drive frequencies, a different type of time-dependent pattern commonly appears, which has random components in both space and time. Figure 13 shows sequential images of such disordered silent discharge patterns for level II. The time interval between successive images is $\frac{1}{30}$ sec and the control parameters are $V_b = 250$ V, $f_{dr} = 1$ kHz. As shown, this type of pattern exhibits temporal correlation and some hexagonal order. As the drive frequency increases at fixed V_b, the pattern

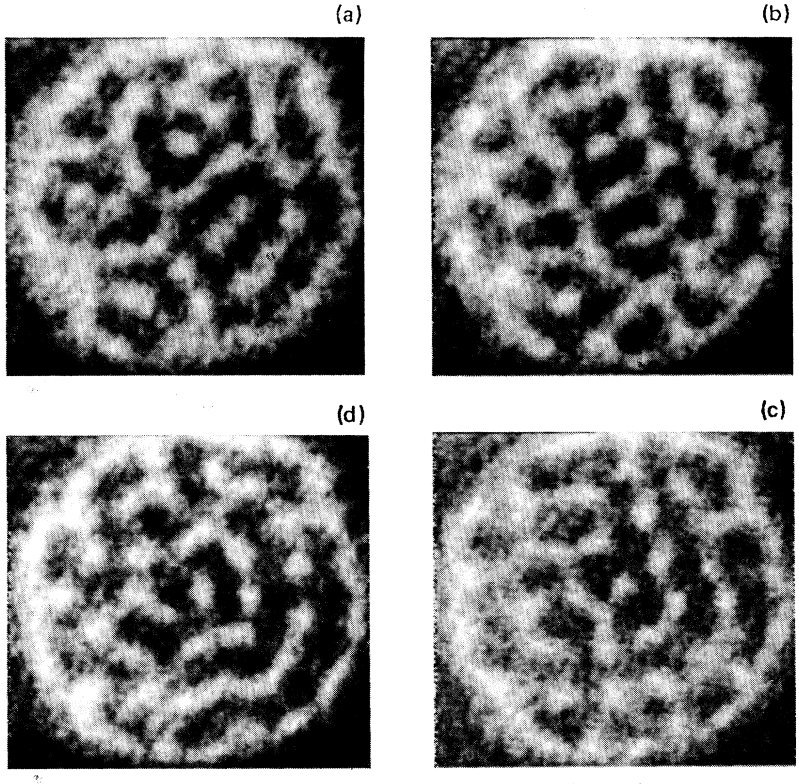

FIG. 13. Four sequential pictures of a disordered time-dependent state at level II. Pictures are separated by $\frac{1}{30}$ sec ($V_b = 250$ V, $f_{dr} = 1$ kHz).

eventually becomes a static hexagonal lattice.

The quasirandom appearance of low f_{dr} silent discharge patterns of the type shown in Fig. 13 probably results from the nearly complete smoothing, by drift and diffusion, of lateral space-charge inhomogeneities in the long times between current pulses. This space charge plays an important role in the stability of ordered patterns, as discussed above. As the drive frequency is lowered and the space charge weakens, the effects of random charge density fluctuations on the lateral location of current avalanches are enhanced, and lowering the drive frequency effectively increases the noise in the system. Although it is possible that these noisy patterns represent deterministic spatiotemporal chaos, we find that they occur *only* for low drive frequencies and voltages, which we expect to increase the importance of fluctuations in the system, while regions of deterministic chaos typically occupy islands in parameter space. For all impurity levels and sufficiently low drive frequencies, we expect space-charge smoothing to produce such "noisy" patterns, which we do observe at levels II, III, and IV. At level I the wavelength of the pattern is nearly the same as the cell's diameter, so a larger cell would be required to see noisy patterns that resemble Fig. 13.

The partially stochastic patterns in Fig. 13 are interesting because they show a strong influence of random fluctuations on patterns in a spatially extended nonequilibrium system. The effects of fluctuations in such systems are an important topic that remains poorly understood. Recently, mesoscopic simulations of nonequilibrium chemical reactions have been made that include fluctuations in a lattice-gas automaton model [15]. The results of these simulations of Turing patterns closely resemble Fig. 13, which is typical of the type of silent discharge pattern that we find in the low-drive-frequency regime.

In conclusion, we have found that silent discharges exhibit an extremely rich variety of both static and time-dependent patterns. The type of pattern that the discharge displays is sensitive to the drive frequency and voltage, to the gap height, and to the pressure and composition of the gas. For low impurity levels in He, the silent discharge forms static patterns similar to the Turing patterns observed in nonequilibrium chemical reactions. For much of parameter space, the sequence of bifurcations between the different static pattern types follows the order *uniform* $\rightarrow$ *hexagonal* $\rightarrow$ *striped,* as in amplitude equation models of systems that form hexagonal patterns. For higher impurity levels, we observe several different types of patterns with persistent time dependence, including low-drive-frequency, disordered patterns that appear to be sensitive to fluctuations in the space-charge density. The rich behavior, simple visualization, and convenient experimental time scales of silent discharges make them well suited to further studies of two-dimensional patterns in nonequilibrium systems.

[1] S. Ciliberto, E. Pampaloni, and C. Perez-Garcia, Phys. Rev. Lett. **61**, 1198 (1988).

[2] M. Ohgiwari, M. Matsushita, and T. Matsuyama, J. Phys. Soc. Jpn. **61**, 816 (1992).

[3] Q. Ouyang and H. L. Swinney, Nature **352**, 610 (1991).

[4] M. C. Cross and P. C. Hohenberg, Rev. Mod. Phys. **65**, 851 (1993).

[5] C. Radehaus *et al.*, Phys. Rev. A **42**, 7426 (1990).

[6] dc glow discharge patterns in a gas-filled narrow gap between a quasi-1D copper electrode and a quasi-1D doped semiconductor have been studied by C. Radehaus *et al.* See [5].

[7] C. Radehaus, H.Willebrand, R. Dohmen, F. J. Niedernostheide, G. Bengel, and H. G. Purwins, Phys. Rev. A **45**, 2546 (1992).

[8] B. Eliasson and U. Kogelschatz, IEEE Trans. Plas. Sci. **19**, 1063 (1991).

[9] Ozone is used, e.g., for the purification of drinking water.

[10] B. Eliasson, M. Hirt, and U. Kogelschatz, J. Phys. D **20**, 1421 (1987).

[11] H. Esrom and U. Kogelschatz, Appl. Surf. Sci. **54**, 440 (1992).

[12] U. Kogelschatz, Pure Appl. Chem. **62**, 1667 (1990).

[13] D. G. Boyes and W. A. Tiller, J. Appl. Phys. **44**, 3102 (1973).

[14] E. Ammelt, D. Schweng, and H. G. Purwins, Phys. Lett. A **179**, 348 (1993).

[15] R. Kapral, A. Lawniiczak, and P. Maisiar, Phys. Rev. Lett. **66**, 2539 (1991).

[16] Q. Ouyang, Z. Noszticius, and H. L. Swinney, J. Phys. Chem. **96**, 6773 (1992).

[17] Corning Microsheet.

[18] E. Nasser, IEEE Spectrum **5**, 127 (1968).

[19] O. Sahni, C. Lanza, and W. E. Howard, J. Appl. Phys. **49**, 2365 (1978). The impact of positive ions at the dielectric surfaces produces a flux of secondary electrons that depends on the incident ion flux and the dielectric composition. Both surfaces may also originate electrons through photoemission.

[20] The breakdown field depends on the *Pd* product of the gas pressure P and the gap height d (Paschen's law). See [21].

[21] E. Nasser, *Fundamentals of Gaseous Ionization and Plasma Electronics* (Wiley, New York, 1971).

[22] S. K. Dhali and P. F. Williams, J. Appl. Phys. **62**, 4696 (1987).

[23] All of these parameters are pressure dependent. For silent discharges, n_e and n_+ are 10^{-7}–10^{-6} times smaller than the neutral species density n_0.

[24] L. B. Loeb, *Basic Processes of Gaseous Electronics* (University of California Press, Berkeley, 1955).

[25] W. Egli and B. Eliasson, Helv. Phys. Acta **65**, 127 (1992).

[26] For typical silent-discharge parameters, the duration of the transient current flow is ~ 1 nsec. See [10].

[27] This expression assumes that the charge accumulates in sheets at the dielectric surfaces and does not take into account the spatial distribution of the electron and ion densities, which vary both laterally and in the z direction normal to the electrodes.

[28] The avalanche breakdown can proceed by two mechanisms: by streamer breakdown if the applied field varies

rapidly enough in time or if $n_0 d$ is large and the coefficient γ for secondary electron ejection from the dielectric surface is small. Townsend breakdown may also occur if $n_0 d$ is small and the field bias varies slowly. See [29].

[29] B. Eliasson and U. Kogelschatz (unpublished).

[30] $\alpha = An_0 \exp(-\beta n_0/E)$, where A and β are constants that depend on the gas's ionization potential, and n_0 is the gas density. See [22].

[31] This effect is very pronounced for streamers, but is also relevant under Townsend breakdown conditions.

[32] For sufficiently small gap heights; branching discharge avalanches typically form for large d (a few cm) gaps.

[33] S. M. Sze, *Physics of Semiconductor Devices* (Wiley Interscience, New York, 1969).

[34] F. M. Lay, C. K. Chu, and P. H. Haberland, IBM J. Res. Dev. **18**, 244 (1974).

[35] Δt_{smooth} is not simply the dielectric relaxation time of the plasma, because the dielectric sheets influence the mobility of the transferred charge along the glass surfaces.

[36] For very low drive frequencies, discharge avalanches are random in space and time, because the long times between the current pulses allow nearly complete decay of lateral inhomogeneities in the transferred charge σ_g. As the drive frequency increases, the locations of avalanches become correlated in time when Δt_{smooth} is roughly equal to the drive period that gives the $\Delta t_{\text{smooth}} \sim 1-10$ msec estimate above.

[37] S. Ciliberto, J. L. P. Coullet, E. Pampaloni, and C. Perez-Garcia, Phys. Rev. Lett. **65**, 2370 (1990).

[38] B. A. Malomed and M. I. Tribelskii, Zh. Eksp. Teor. Fiz. **92**, 539 (1987) [Sov. Phys. JETP **65**, 305 (1987)].

[39] F. H. Busse, J. Fluid Mech. **30**, 625 (1967).

[40] V. Dufiet and J. Boissonade, Physica A **188**, 158 (1992).

[41] G. Ahlers, L. I. Berge, and D. S. Cannell, Phys. Rev. Lett. **70**, 2399 (1993).

[42] A. Newell, T. Passot, and M. Souli, J. Fluid Mech. **220**, 187 (1990).

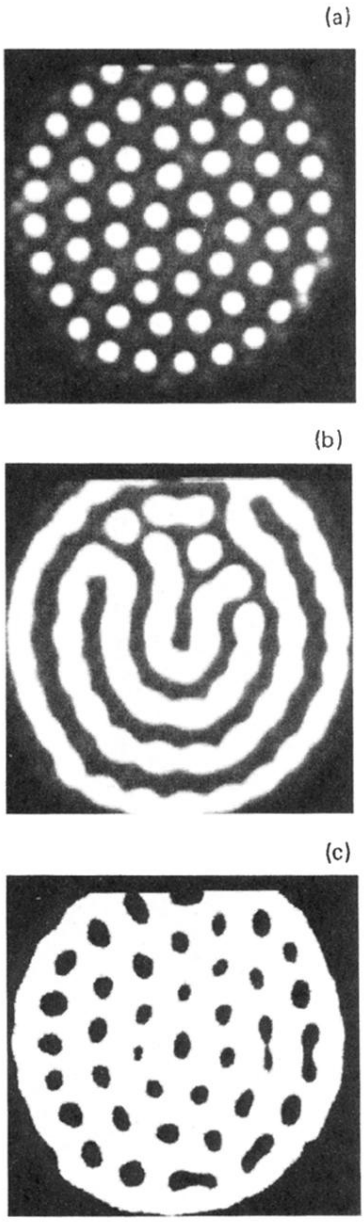

FIG. 10. Patterns at level II ($d = 125$ μm, $P_{He} \sim 300$ Torr, $P_{water} = 200$–800 mTorr). (a) An array of dots ($V_b = 210$ V, $f_{dr} = 100$ kHz). (b) Textured stripe pattern ($V_b = 240$ V, $f_{dr} = 100$ kHz). (c) Inverted dot array ($V_b = 255$ V, $f_{dr} = 100$ kHz).

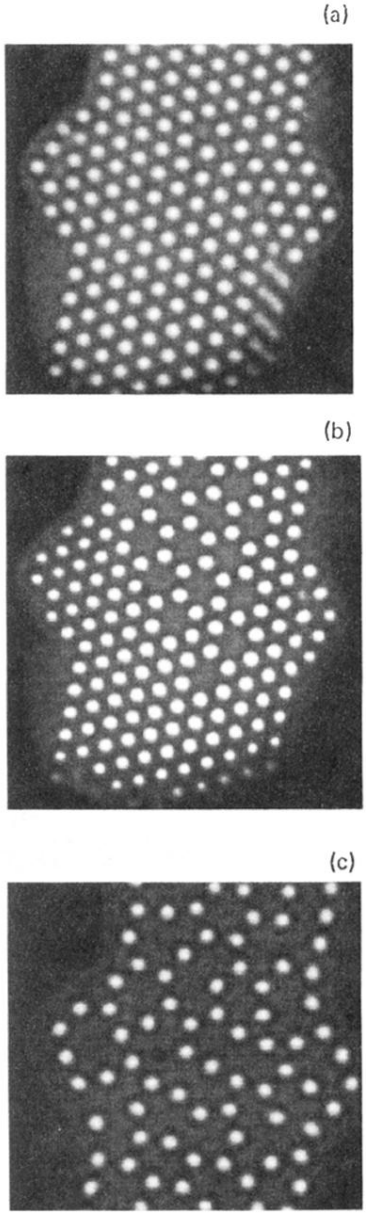

FIG. 11. New pattern types at level IV ($d = 75\ \mu$m, $P_{He} \sim 700$ Torr, $P_{water} = 4$ Torr). (a)–(c) show the reduction in the number of nearest neighbors with increasing impurity level. Patterns (a) and (b) are static and pattern (c) is time dependent. (a) Vacancies appear in the upper right quadrant of the cell ($V_b = 365$ V and $f_{dr}^{*} = 80$ kHz). (b) An open, hexagonal array appears in the central region of the cell ($V_b = 360$ V, $f_{dr} = 180$ kHz. (c) Dynamic pattern of chained dots ($V_b = 365$ V, $f_{dr} = 80$ kHz).

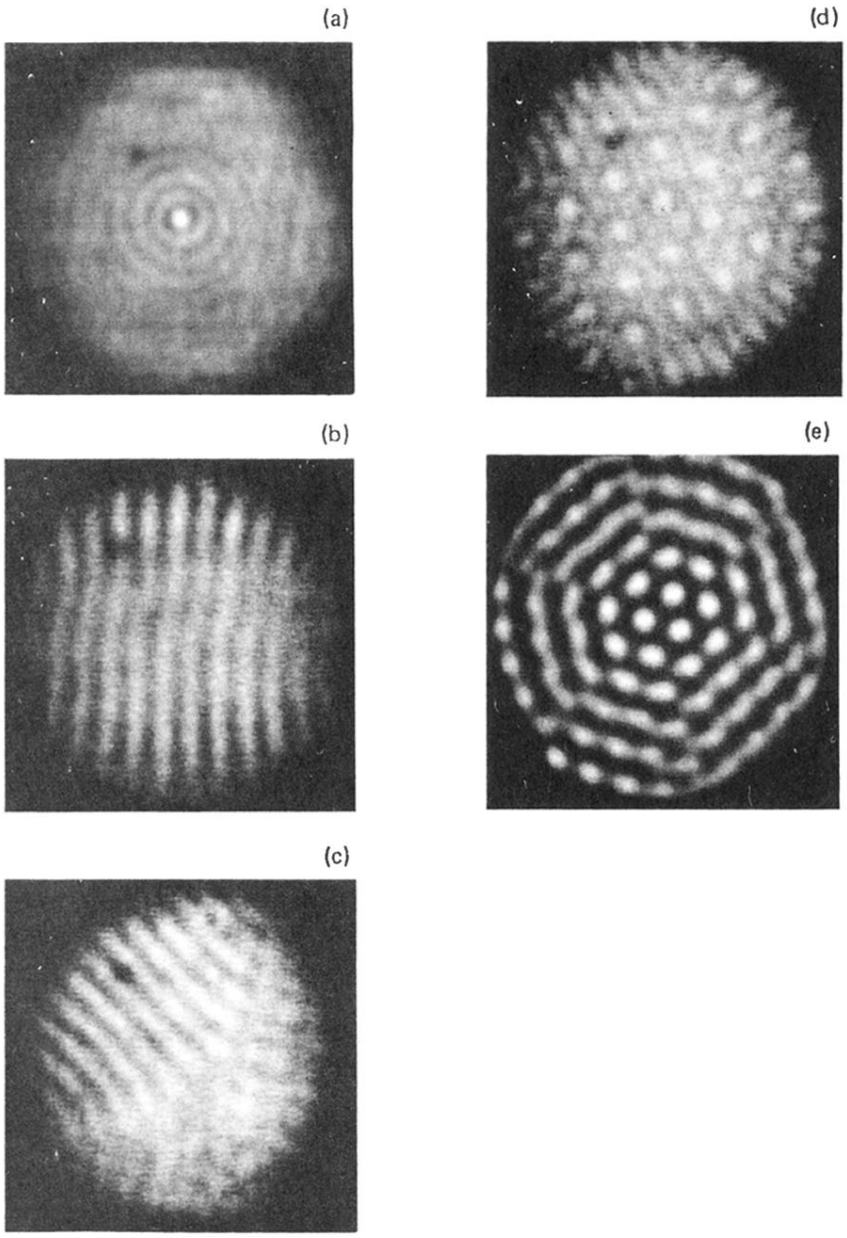

FIG. 12. Time-dependent patterns at level III ($d = 125$ μm, $P_{He} \sim 300$ Torr, $P_{water} \sim 800$ mTorr–1.2 Torr). (a) Target pattern of concentric traveling waves, which are emitted from the central focus (bright spot) for $V_b = 340$ V and $f_{dr} = 190$ kHz. (b),(c) Dynamic stripe pattern that rapidly reorients between different preferred axes ($V_b = 340$ V and $f_{dr} = 180$ kHz). (d) Dynamic, mixed pattern of stripes and dots ($V_b = 400$ V and $f_{dr} = 180$ kHz). (e) Rapidly rotating hexagonal dot pattern ($V_b = 260$ V and $f_{dr} = 180$ kHz).

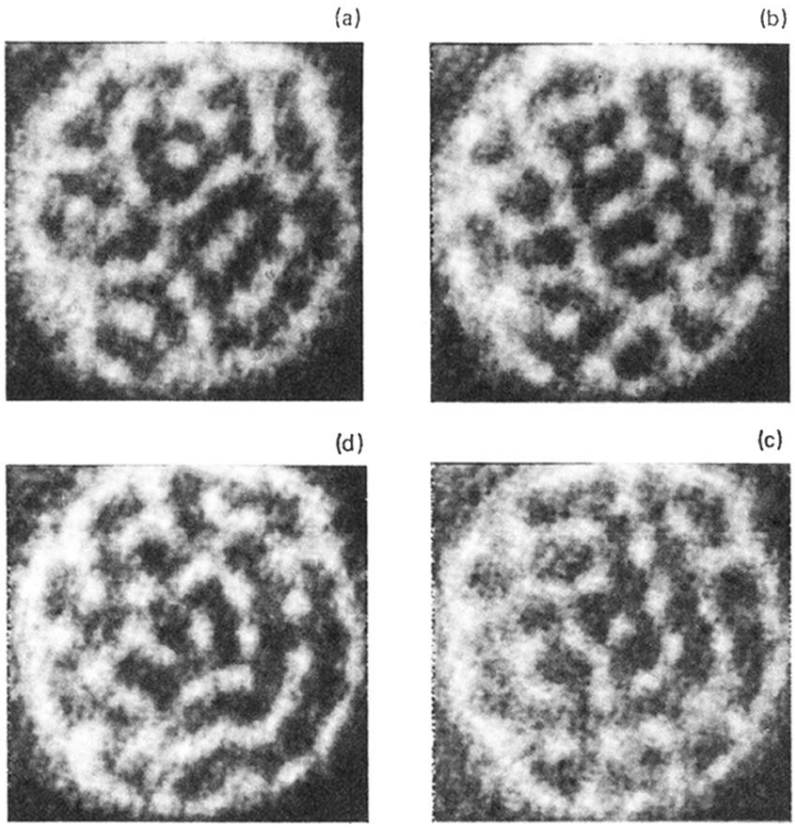

FIG. 13. Four sequential pictures of a disordered time-dependent state at level II. Pictures are separated by $\frac{1}{30}$ sec ($V_b = 250$ V, $f_{dr} = 1$ kHz).

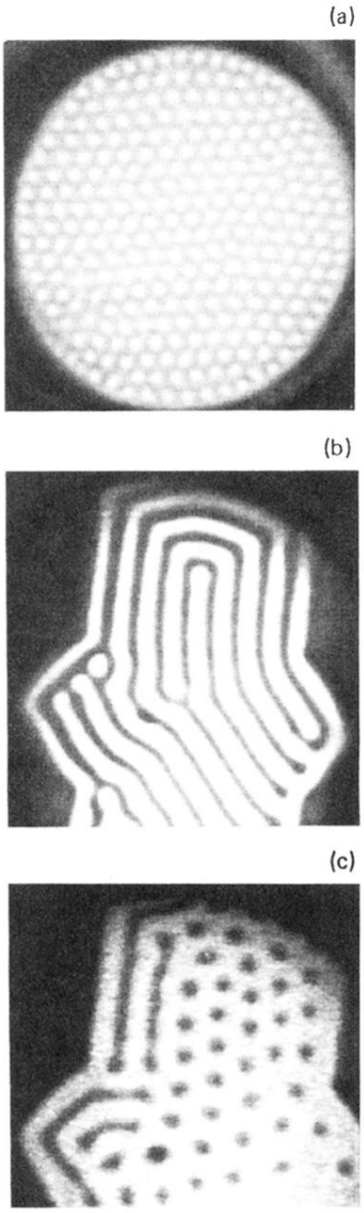

FIG. 6. Patterns formed at level I ($d = 75$ μm, $P_{He} \sim 700$ Torr, $P_{H_2O} < 60$ mTorr). The discharge area is circular in (a) and has a rhombus-shaped region between rectangular sections in (b) and (c). (a) Hexagonal pattern of bright dots ($V_b = 400$ V, $F_{dr} = 80$ kHz). (b) Stripe pattern ($V_b = 350$ V, $f_{dr} = 45$ kHz). (c) inverted hexagonal array (right-hand side) and stripes (left-hand side), for $V_b = 320$ V and $f_{dr} = 6$ kHz. The symbols within the regions correspond to the points at which data were collected.